3D reconstruction of sub-wavelength scatterers from the measurement of scattered fields in elastic waveguides

Ludovic Moreau[1,2], Alan J. Hunter[3], Alexander Velichko[4]
Paul D. Wilcox [4]

Abstract

In non-destructive testing, being able to remotely locate and size defects with good accuracy is an important requirement in many industrial sectors such as petrochemical, nuclear and aerospace.The potential of ultrasonic guided waves is well known for this type of problem, but interpreting the measured data and extracting useful information about the defects remains challenging. This paper introduces a Bayesian approach to measuring the geometry of a defect while providing at the same time an estimate of the uncertainty in the solution. To this end, a Markov-Chain Monte Carlo algorithm is used to fit simulated scattered fields to the measured ones. Simulations are made with efficient models where the geometry of the defects are provided as input parameters, so that statistical information on the defect properties such as depth, shape and dimensions can be obtained. The method is first investigated on simulations to evaluate its sensitivity to noise and to the amount of measured data, and it is then demonstrated on experimental data. The defect geometries vary from simple elliptical flat-bottomed holes to complex corrosion profiles.

Index Terms

NDE, Guided wave, MCMC, Bayesian, Imaging

1. Author is with the Univ. Grenoble Alpes, ISTerre, F-38041 Grenoble, France. email: ludovic.moreau@ujf-grenoble.fr
2. Author was also with the CEA - LIST, 91191 Gif-sur-Yvette, France
3. IEEE Member. Author is with TNO, Oude Waalsdorperweg 63, 2597 AK The Hague, The Netherlands
4. Author is with the Department of Mechanical Engineering, University of Bristol, Bristol BS8 1TR, United Kingdom

I. Introduction

ULTRASONIC guided waves (GW) are well suited for non-destructive inspection due to their capacity to propagate over many wavelengths while being sensitive to the geometrical and the elastic properties of the waveguide. Their potential has been used for many years in non-destructive evaluations (NDE) [1], and also more recently in the field of biomedical acoustics for the evaluation of bone properties [2]. In NDE, typically inspections are made by sending a GW onto the region to detect and, if present, characterize defects based on measurements of the scattered wave. The frequency is generally limited to a bandwidth were only the fundamental modes propagate so that the relative amplitude of these modes can be measured. Thanks to the completeness of the GW basis [3], every defect has a scattered field with unique modal amplitude and directivity. If one is able to measure the full scattered field of a defect, then in principle all its geometrical characteristics can be extracted from the data.

In practice, recovering useful information about a defect directly from the scattered field is very challenging, mainly because (i) accessing the full scattering pattern is generally not possible, (ii) signal-to-noise may be very poor, (iii) it is not clear how to extract the pertinent information in a robust way, and (iv) the problem is not guaranteed to be well posed, since two particular types of defect with very different implications for structural integrity may have similar scattering patterns. For these reasons, past investigations have focused mainly on the forward problem where the influence of the defect geometry on the scattered field is studied. Predoi *et al* studied the reflection and transmission coefficients from surface opening defects [4], Carandente et *al* studied the influence of sharp changes in the geometry of a scatterer on the reflection of GW [5], Lovstad and Cawley investigated reflections of GW from pit clusters in pipes [6], Mi *et al* investigated the initiation and growth of fatigue

cracks based on dynamic monitoring [7].

Recent attempts to GW imaging allowed successful localization of scatterers in a waveguide. Velichko *et al* used the full matrix capture of transmit/receive signals to image defects of variable size in a pipe using the back-propagation method [8]. Bourgeois and Luneville applied the linear sampling method for the 2D imaging of reflectors [9]. While the detection and localization of a defect is possible, recovering accurate informations about its geometry is still out of reach of conventional GW methods. From an NDE point of view, this is problematic in many industrial applications. For example, in the oil and gas industry, being able to remotely locate and size corrosion defects remains an important preoccupation. Such defects are particularly difficult to characterize due to the complexity of the corrosion geometry itself, and the fact that the most important characteristic required from a structural integrity perspective is often the maximum depth of localized pits or cracks within a corroded region [10].

Identifying a reliable and robust method that is able to characterize defects directly from their scattered field is desirable. Inverse methods that consist of matching the output data of a model to experimentally measured data appear like reliable candidates, provided that computational costs remain reasonable. In these methods, a measure of the error between the model and the experiments is generally defined and the parameters in the model (*e.g.* the geometrical parameters of the defect) are varied in order to minimize this error. Singh and Castaings used a 2D finite element (FE) model to fit measurements of reflection and transmission coefficients of strip-like defects defined with 2 geometrical parameters [11]. The defects were characterized with the least squares method after all possible combinations of parameters were tested. However, this is not a viable approach for realistic defects with a complicated geometry because the parameter search space is multidimensional.

A potentially more tractable solution consists of using a Bayesian approach, for example via the Markov Chain Monte Carlo (MCMC) computational method. Although MCMC methods are used in various research fields such as physics [12], biology [13], economics [14], and even neural sciences [15], so far their application to NDE has remained limited. Khan used MCMC for inverse problems in electromagnetic NDE [16], and Zhang *et al* used the Metropolis-Hastings algorithm to evaluate grain orientation in a weld [17]. Other investigations concern mostly data fusion and probability of detection [18]-[20].

A model-based data fitting method for Bayesian inference requires a significant number of simulations to extract reliable statistical information. Without efficient forwards models, such approaches become computationally prohibitive. This paper introduces an MCMC method combined with either an analytical [21], [22] or an efficient FE model [23]-[25] to estimate the full 3D geometry of sub-wavelength defects in plate-like structures with stress-free boundary conditions and 3D elasticity (section II). To investigate the robustness of the method, it is tested first on data obtained from simulated experiments where the noise level and the amount of collected data can be controlled (section IV). The simulation study is made on flat-bottomed, partly through-thickness holes with an elliptical contour. Then the accuracy of the method is tested on two simulated defects with complex geometries caused by actual corrosion. Finally, the approach is applied to experimental data collected in an aluminium plate with a hand-drilled flat-bottomed hole (section V).

II. Bayesian procedure for the characterization of the scatterer

A. Model-based data fitting

Consider frequency-domain experimental data resulting from the interaction of a guided mode with a scatterer in an elastic waveguide that supports Lamb wave-like propagation (plate, pipe...). We assume the frequency to be such that only the 3 fundamental

modes, S_0, SH_0 and A_0 can propagate, higher order modes being evanescent. The resulting scattered field can be written in the form of the scattering matrices of the 3 modes: $\hat{\mathcal{S}} = \{\hat{S_0}^{\phi}(\theta), S\hat{H_0}^{\phi}(\theta), \hat{A_0}^{\phi}(\theta)\}$. The scattering matrix describes the amplitude of the modes in the far field of a scatterer for any combination of incident (ϕ) and scattering (θ) angles [26]. Given any incident angle ϕ, if the scattered field of the 3 modes can be measured all around the defect, then a 1:1 relationship exists between sets of the scattering matrices (for all 3 modes at this particular incident angle) and the defect geometry thanks to the completeness of the GW basis [3]. The minimum number of scattering angles N_θ to obtain independent information about the scatterer depends on the wavelength of the scattered mode, λ_{in}, and on the maximum dimension of the scatterer, D, such that [27]:

$$N_\theta = \frac{2\pi D}{\lambda_{in}}. \tag{1}$$

Eq. (1) was derived from Nyquist's sampling criterion. A consequence is that in theory, as long as the scattering pattern of the 3 propagating modes can be measured around the scatterer with an angular sampling that satisfies this formula, only one incident angle is required in the scattering matrix for the inverse problem to be well-constrained.

Assuming the experiment can be modeled faithfully, the basic idea of our approach is that if the output data of the model fits the measurements in the above mentioned conditions, then the geometrical parameters in the model describe the defect adequately. In practice, however, generally only a restricted number of modes and/or scattering angles, θ_j, are available experimentally. In that case, the uniqueness of the solution can't be guarantied unless additional data can be gathered (more incident angles, a different frequency of inspection...). A full investigation on that matter is not presented in this paper, but an empirical study of how well the inversion procedure performs in that case is presented in section IV-A.

Let us introduce $\mathbf{X}$, the variable that contains the geometrical parameters of the scatterer

in the model:

$$\mathbf{X} = \{p_1, p_2, ..., p_M\}^T, \tag{2}$$

where $p_m \in P_m$, the search space associated with parameter m. M is the number of parameters.

Next, the position of the defect is described in the Cartesian coordinates system (O, x, y, z) with origin O. To express the scattered field around the defect a cylindrical coordinates system, (O, r, θ, z), is also introduced. The polar coordinates (r, θ) are related to the Cartesian coordinates (x, y) such that $r^2 = x^2 + y^2$ and $\cos\theta = x/r$. Assume that a guided wave with a plane wavefront is incident on a cavity, in a direction that makes an angle ϕ with the x axis, and that measurements are made at a distance R_0 from the origin, at J discrete positions θ_j. Under this notation, the error between the measured and the modeled data can be expressed in terms of the root mean square (RMS) such that:

$$\left(\chi^{\phi}\right)^2(\mathbf{X}) = \frac{1}{3}\sum_{j=1}^{J}\left[\left(\hat{S_0}^{\phi}(\theta_j) - S_0^{\phi}(\theta_j)\right)^2 + \left(\hat{SH_0}^{\phi}(\theta_j) - SH_0^{\phi}(\theta_j)\right)^2 + \left(\hat{A_0}^{\phi}(\theta_j) - A_0^{\phi}(\theta_j)\right)^2\right], \tag{3}$$

where $\mathcal{S} = \{S_0^{\phi}(\theta_j), A_0^{\phi}(\theta_j), SH_0^{\phi}(\theta_j)\}$ denote the scattering matrices of the 3 fundamental modes in the model.

Therefore in the examples of sections IV and V the geometry of the defect will be calculated with only 1 incident angle. However, when data from only a limited range of scattering angles is accessible, and/or when not all modes are measured, then using more incident angles can improve the accuracy of the solution. This will be demonstrated next.

Obviously, more complicated defect geometries will necessitate more model parameters for an adequate representation of the geometry. When the number of parameters becomes too high, minimizing $\chi^{\phi}(\mathbf{X})$ may require a prohibitive number of calculations. For example, consider a flat-bottomed defect with an elliptical contour. 4 parameters are required to

describe its geometry: depth, minor and major axes, and orientation with respect to the incident wave. In a brute-force exhaustive search of the parameter space meshed with 20 different values for each dimension, the model must be run for a number of times equal to $20^4 = 160000$ combinations. Even with efficient modeling, this inversion method would be intractable using current computing technology. A more tractable way of minimizing the error is to proceed with a classical gradient descent. However, unless the first guess of the solution is sufficiently close to the global minimum, this process is likely to become stuck at local minima. Next, it will be demonstrated that a Bayesian approach can overcome these difficulties and provide an estimate of the geometrical features of a defect with very good accuracy while running a much smaller number of forward model evaluations, by comparison to an exhaustive search.

Bayesian estimation is based on the principle that the set of parameters in an estimation problem can be quantified by probability distributions. Bayes' theorem offers a framework for evaluating these distributions from direct or indirect and imperfect measurements of the parameter space. The advantage of the approach is two-fold. Firstly, it is robust to measurement errors since these can be quantified and accounted for in a statistically optimal sense. Secondly, not only can estimates of the parameters be obtained via expectations of the distributions, but the uncertainties of these estimates can be quantified by higher-order moments, thus revealing potential non-unique solutions. In particular, this second advantage adds considerable value in NDT applications by providing a quantitative metric for confidence in the solution.

Using Bayes' theorem, the posterior distribution of the parameter values is given by

$$P(\mathbf{X}|\hat{\mathcal{S}}) = \frac{P(\hat{\mathcal{S}}|\mathbf{X})P(\mathbf{X})}{P(\hat{\mathcal{S}})}, \tag{4}$$

where $P(\hat{\mathcal{S}}|\mathbf{X})$ is the likelihood function, $P(\mathbf{X})$ is the prior distribution and $P(\hat{\mathcal{S}})$ is the

marginal likelihood function or the model evidence. The posterior distribution expresses the conditional probability of the parameter values based on evidence from measurements, expressed by the likelihood function, and from prior assumptions, expressed by the prior distribution. A recurrent problem in Bayesian inference is the difficulty to calculate the marginal likelihood, which is essentially a normalization factor. However, because it is the same for all probabilities, its determination is not necessary in practice, since it can be cancelled by comparing ratios of probabilities rather than probabilities themselves. This is one of the motivations for using methods based on stochastic sampling such as MCMC.

B. The Metropolis-Hastings algorithm

The Metropolis-Hastings algorithm is one of several algorithms that can be used to evaluate the Bayesian posterior distribution by realizing a Markov chain in the parameter search space. This random walk satisfies the ergodic theorem, which allows the algorithm to converge towards a stationary state that approximates the posterior distribution [28]. In the present problem, it is assumed that measurement errors are uncorrelated, random and therefore can be modeled by a normal distribution. Thus, a zero-mean Gaussian likelihood function with variance σ^2 is prescribed:

$$P(\hat{\mathcal{S}}|\mathbf{X}) = \exp\left(-\frac{\left(\chi^{\phi}\right)^2(\mathbf{X})}{2\sigma^2}\right), \tag{5}$$

This is a typical likelihood function used in many data fitting problems [29]. Furthermore, it is assumed for the prior distribution that the model parameters p_m have equal probability over a finite range of values $[p_{m,min}, p_{m,max}]$:

$$P(p_m) = \left\{ \begin{array}{cc} \frac{1}{p_{m,max}-p_{m,min}}, \forall\ p_m \in [p_{m,min}, p_{m,max}] \\ 0, \qquad\qquad \text{elsewhere} \end{array} \right\} \quad \text{and} \quad P(\mathbf{X}) = \prod_m P(p_m). \tag{6}$$

The algorithm is initialized with a solution $\mathbf{X^0} = \{p_1^0, p_2^0, ..., p_M^0\}^T$, and then iterates via the following steps:

1) Based on the previously accepted solution, $\mathbf{X^{n-1}}$, define a candidate solution $\mathbf{X^{cand}}$ for the defect geometry by randomly altering the parameters of $\mathbf{X^{n-1}}$ such that

$$\mathbf{X^{cand}} = \mathbf{X^{n-1}} + \Delta\mathbf{X}(n), \tag{7}$$

where $\Delta\mathbf{X}(n) = \{\Delta p_1(n), ..., \Delta p_M(n)\}^T$ is the step size in the Markov chain. $\Delta p_m(n)$ is a fraction of the search space associated with parameter p_m. Its size depends on the iteration (see section II-C).

2) Use the forward model to evaluate the scattered field from this candidate.

3) Estimate the likelihood of the candidate $P(\hat{\mathcal{S}}|\mathbf{X^{cand}})$.

4) If the candidate is more likely than the previous accepted solution, then it is accepted, otherwise it is accepted with probability $\frac{P(\hat{\mathcal{S}}|\mathbf{X^{cand}})}{P(\hat{\mathcal{S}}|\mathbf{X^n})}$. This is equivalent to accepting the candidate if

$$\alpha \leq \min\left[1, \frac{P(\hat{\mathcal{S}}|\mathbf{X^{cand}})}{P(\hat{\mathcal{S}}|\mathbf{X^n})}\right], \tag{8}$$

where α is a random number sampled between 0 and 1 from a uniform distribution.

5) If the candidate is accepted, then the algorithm moves to the new solution, and $\mathbf{X^{cand}}$ is added to the chain $[\mathbf{X^0}, \mathbf{X^1}, ...\mathbf{X^{n-1}}]$, otherwise the algorithm stays at $\mathbf{X^{n-1}}$.

In the resulting Markov chain, sets of consecutive accepted parameters are correlated. Assume that the Markov chain has stabilized after n_P solutions, and the remainder of the chain contains N_P solutions $[\mathbf{X^{n_P}}, \mathbf{X^{n_P+1}}, ...\mathbf{X^{n_P+N_P-1}}]$. To obtain statistically independent samples with which to estimate the posterior distribution of parameters from the Markov chain, solutions are sampled every J accepted sets, $[\mathbf{X^{n_P}}, \mathbf{X^{n_P+J}}, \mathbf{X^{n_P+2J}}, ...]$, where J exceeds the correlation length of the sequence. Typically, in $\mathbf{X^{n_P...N_P}}$ the correlation coefficients of all consecutive sequences of length J are evaluated. This operation is repeated for increasing

values of J, until the correlation coefficients stabilize under a value low enough to assume uncorrelated samples, which indicates statistically independent data. For the present problem, it was observed that independent samples can be assumed around $J = 30$. In order to be sure that correlations lengths are exceeded in all examples, J was heuristically set to a higher value of 50. Finally the expected parameters values are calculated from the mean of these samples:

$$\hat{\mathbf{X}} = \frac{J}{N_P} \sum_k \mathbf{X}^{\mathbf{nP+kJ}}. \tag{9}$$

C. Speeding up convergence by simulated annealing

Generally a number of iterations are necessary for convergence of the MCMC algorithm, and the efficiency of this method depends on the duration of this burn-in phase. It is however not possible to know *a priori* the number of iterations necessary for convergence, because it is influenced by

i) the sensitivity of the algorithm to parameters changes which strongly depends on the physics of the problem;

ii) the step size in the Markov chain;

iii) the extent of the likelihood function, σ^2 in Eq. (5), which is determined from an estimate of the measurement error (*e.g.* due to noise level or any other source of uncertainty).

A narrow extent or large step size reduces the opportunity for randomly selected samples to yield significant probability values and results in a low chance of acceptance in the MCMC procedure. This may cause the algorithm to have a long convergence period.

Consequently, for faster convergence it is best to start with a first guess close to the global minimum. This can be achieved by running a simulated annealing global optimization [30] before the burn-in stage of the Metropolis-Hastings algorithm. Simulated annealing is also an MCMC method and follows a similar procedure to the Metropolis-Hastings algorithm.

However, its aim is to converge on the global optimum rather than generating samples from the posterior distribution. To this end, both the step size of the Markov chain and the extent of the acceptance probability function (analogous to the likelihood function in the Metropolis-Hastings algorithm) are initialized with large values to allow broad sampling of the parameter space. These values are slowly reduced with each iteration in what is termed the "cooling schedule", and, if a sufficiently gradual schedule is chosen, the algorithm will converge to the global optimum. In the examples of the sections IV and V, the simulated annealing is started from a position defined randomly in the search space, generally far from the global minimum.

In practice, the cooling schedule can be implemented in a number of ways. In this study, a standard schedule is implemented over a number N_a of iterations, where the variance of the Gaussian acceptance function is reduced from $T_1 = 10\sigma^2$ to $T_{N_a} = \sigma^2$, and the step size from a value of $T_1 = \frac{\sup(P_m)-\inf(P_m)}{2}$ to $T_{N_a} = \frac{\sup(P_m)-\inf(P_m)}{50}$. $\mathrm{Sup}(P_m)$ and $\inf(P_m)$ denote the supremum and infimum of the parameter search space P_m, respectively. The cooling schedule, T, is an exponential function that varies between these values such that:

$$T = \begin{cases} T_1 \left(\frac{T_1}{T_{N_a}}\right)^{n/N_a}, \text{ if } n \leq N_a \\ T_{N_a}, \text{ if } N_a < n \leq N. \end{cases} \tag{10}$$

For example, if parameter m is the depth of the defect, the associated search space is $P_m = [0; 100\%]$ and the step size varies from 50% at the first iteration to 2% at the last one. At the end of the simulated annealing, the procedure enters the Metropolis-Hastings algorithm and both the step size and the likelihood function are kept constant.

III. Forward modelling

Full 3D modeling of GW scattering problems has been made possible in recent years thanks to the constant increase in computational power. However the Bayesian approach

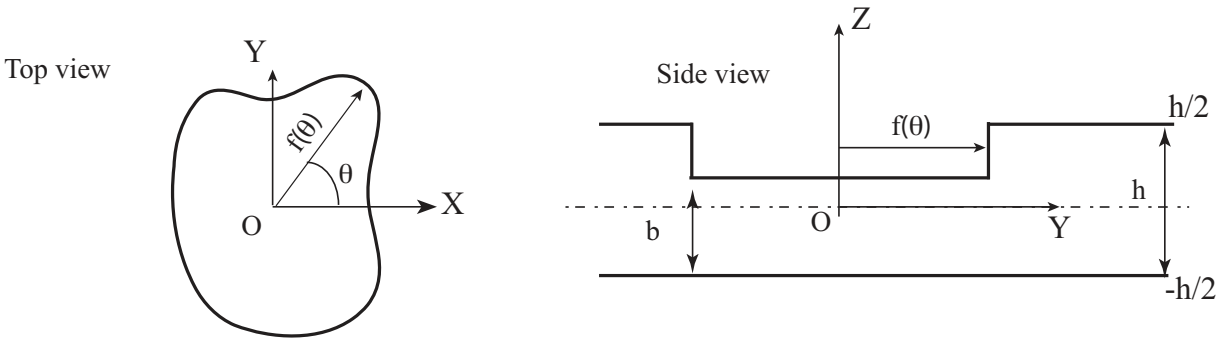

Fig. 1. Configuration and notations in the analytical model

described in section II.A typically requires between 10000 and 20000 iterations to collect enough data for statistical moments to be calculated. Without an efficient model, computations would still require powerful machines and calculation times would remain prohibitive for an inversion using the Metropolis-Hastings algorithm. Recently, an analytical model was introduced for the scattering of flat-bottomed cavities with an irregular contour [22]. An efficient FE model valid for any geometry of scatterer was also developed [8]. These models are used in this paper for the various simulations and are then briefly described in this section.

A. Analytical model

Consider a flat-bottomed hole in a plate of thickness h. The thickness of the thinner plate under the hole is denoted b. Assume that the θ-dependent radius of the hole, r, can be expressed with a function once differentiable, f (figure 1). When a guided wave is incident with a planar wavefront on the cavity in the harmonic regime at a given frequency, the boundary conditions associated with the problem are such that:

$$\begin{cases} \mathbf{S}^{sc}(z,\theta)\mathbf{n}(\theta) = -\mathbf{S}^{in}(z,\theta).\mathbf{n}(\theta), & -h/2+b < z < h/2, \quad r = f(\theta) \\ [\mathbf{S}^{sc}(z,\theta) - \mathbf{S}^{st}(z,\theta)]\,\mathbf{n}(\theta) = -\mathbf{S}^{in}(z,\theta).\mathbf{n}(\theta), & -h/2 < z < -h/2+b, \quad r = f(\theta), \\ \mathbf{u}^{sc}(z,\theta) - \mathbf{u}^{st}(z,\theta) = -\mathbf{u}^{in}(z,\theta), & -h/2 < z < -h/2+b, \quad r = f(\theta). \end{cases} \tag{11}$$

where $\mathbf{S}$ and $\mathbf{u}$ denote the stress tensor and displacement vector of the acoustic fields, respectively. Superscripts *in*, *sc* and *st* refer to the incident field, the scattered field and the standing field beneath the cavity, respectively. $\mathbf{n}$ is the outward normal to the scatterer. The stress and displacement fields in this equation depend on the z coordinate due to the different mode shapes, and on the θ coordinate due to the non-circular geometry of the cavity. Therefore direct inversion of this system is not possible. To solve this problem, a projection method is used according to the following steps.

1) The acoustic fields are expressed in terms of a modal decomposition, where propagating and evanescent modes are included:

$$\mathbf{S}(z,\theta) = \sum_j \mathbf{S^j}(z,\theta) \text{ and } \mathbf{u}(z,\theta) = \sum_j \mathbf{u^j}(z,\theta); \tag{12}$$

2) The θ-dependent functions in Eq. (12) are expanded into Fourier series:

$$\mathbf{S^j}(z) = \sum_k \tilde{\mathbf{S}}^{\mathbf{j}}_{\mathbf{k}}(z) e^{\mathrm{i}k\theta} \text{ and } \mathbf{u^j}(z) = \sum_k \tilde{\mathbf{u}}^{\mathbf{j}}_{\mathbf{k}}(\mathbf{z}) e^{\mathrm{i}k\theta}, \tag{13}$$

where i is the complex number such that $\mathrm{i}^2 = -1$.

3) The resulting boundary conditions are projected onto a basis of appropriate projection functions $P(z,\theta)$ to transform the dependency on z and θ into a set of coefficients.

4) The projected boundary conditions are expressed in the form of a system of linear equations $\mathbf{Aa} = \mathbf{B}$ where the unknowns $\mathbf{a}$ are the modal amplitudes, $\mathbf{B}$ is a vector related to the incident field, and $\mathbf{A}$ is a matrix related to the scattered and standing fields. The resulting system can then be inverted to calculate the elastic field in the plate.

This model allows problems with flat-bottomed holes that have a non-circular contour to be solved, *e.g.* an ellipse or even an irregular shape. For a detailed description of this model, including invertibility of the matrix and stability of the approach, the reader is invited to refer to refs. [21] and [22].

B. Efficient finite element model

In this section the main aspects of the efficient FE model [25] are briefly described. The objective of the modeling process is to deduce the scattered field at any point from a finite-sized, arbitrary shaped scatterer in any incident wavefield. If the boundary of the scatterer is stress free then the boundary condition $S_{ik}^{sc}n_k = -S_{ik}^{in}n_k$ on the scatterer's surface can be directly implemented into the FE model. Here $\{S_{ij}\}$ is the tensor notation for the stress tensor $\mathbf{S}$, subscripts "in" and "sc refer to the incident and scattered wavefields, and $\mathbf{n} = \{n_k\}$ is the outward surface normal. Therefore explicit generation of the plane incident wave is not required.

The procedure is based on a numerical implementation of the integral representation formula for an elastic solid (the formal statement of Huygens's principle) along a closed surface C_{sc} that bounds the scatterer. The scattered wave field recorded from a model can be propagated to any point $\mathbf{r}$ outside C_{sc} using expression

$$u_i^{sc}(\mathbf{r}) = \int_{C_{sc}} \left[u_j^{sc}(\mathbf{r}_c)S_{ijk}^G(\mathbf{r},\mathbf{r}_c) - G_{ji}(\mathbf{r},\mathbf{r}_c)S_{jk}^{sc}(\mathbf{r}_c)\right] n_k dC_{sc} \tag{14}$$

where $\mathbf{n} = \{n_k\}$ is the outward surface normal, $\mathbf{G} = \{G_{ij}\}$ the Green's function for an isotropic elastic plate [32], $\mathbf{S}^G = \{S_{ijk}^G\}$ is the stress tensor corresponding to the Green's function. The physical interpretation is that a scattered wavefield outside C_{sc} can be synthesized by the superposition of the fields from appropriate monopole, $\mathbf{G}$, and dipole, $\mathbf{S}^G$, sources on the surface C_{sc}. In practice the dipole sources are implemented as a finite difference approximation of derivatives in the expression for the stress field. In the far field $r \to \inf$ the Green"s function can be written as a sum of different modes as

$$G_{ji}(\mathbf{r},\mathbf{r}_c) = \frac{1}{\sqrt{r}}\sum_q b_q u_i^q u_j^q \exp(-\mathrm{i}k_q \mathbf{r}_c.\mathbf{e}_{sc})\exp(-\mathrm{i}k_q r) \tag{15}$$

where $\mathbf{e}_{sc} = \mathbf{r}/r$, $\mathbf{u}^q$ is mode shape and b_q are some coefficients. Substituting this asymptotic into the integral (14), finally the expression for the far field scattering amplitude (or scattering matrix [23]) can be obtained in the form of superposition of monopoles and dipoles sources on the surface C_{sc}, with amplitudes determined by the displacement field obtained from the FE model. For the detailed derivation of the expression for the scattering matrix, including explicit formulas for the modal coefficients b_q, the reader is referred to ref. [23]

In the previous model [23], [24] the scatterer was surrounded by artificial damping layers in order to absorb the scattered field and prevent it being reflected back onto the scatterer. In this case any boundary conditions (for example, stress-free) on the boundary of the modeling domain, C_{bnd}, can be taken as the scattered field is negligibly small anyway. However, here the model without absorbing region is considered and then appropriate non-reflecting boundary conditions have to be imposed on C_{bnd}. One possible approach is to use the Huygens' principle (14) again, but now as a boundary condition [25]. A similar method of constructing non-reflecting boundary condition for acoustic media was used in Ref. [31]. Such a boundary condition is non-local in space and in the context of FE model, after discretization, can be written as

$$u_i^{sc}(\mathbf{r}_{bnd}) = \sum_{C_{ref}} \sum_j g_{ij}(\mathbf{r}_{bnd}, \mathbf{r}_{ref}) u_j^{sc}(\mathbf{r}_{ref}), \;\; \mathbf{r}_{bnd} \in C_{bnd}, \mathbf{r}_{ref} \in C_{ref} \tag{16}$$

where C_{ref} is some reference surface which encloses the scatterer and coefficients $g_{ij}(\mathbf{r}_{bnd}, \mathbf{r}_{ref})$ depend on the Green's function G_{ij}. Therefore, the wave field at the boundary nodes is represented as a function of the wave field on the reference surface. The detailed description and rigorous mathematical justification of the FE model, in particular, non-reflecting boundary conditions, is out of scope of this paper and will be presented in a separate publication. Note, that validity of FE model in all calculations was verified by analyzing its convergence and by checking the energy balance.

The method described above is based on the knowledge of the Green's function of the media. For an isotropic plate the Green's function can be calculated analytically provided that the dispersion curves and modes shapes are known [32]. Dispersion curves and mode shapes can be generated by using various techniques, for example, semi-analytical finite-element, global matrix or transfer matrix methods. The Green's function is represented as a superposition of different modes, and theoretically all existing modes (propagating and non-propagating) at a given frequency have to be taken into account. However, if the reference surface C_{ref} is located at a distance of several elements from the scatterer, the Green's function expansion can be truncated and only the first few non-propagating modes need be included to provide good accuracy.

IV. Numerical examples

Simulations allow full control over important parameters such as noise, frequency or geometrical features. Therefore they are particularly well suited to evaluate theoretical capabilities and limitations of the method described in section II. In the following examples, the geometry of the scatterer is calculated with 2 or 3 of the fundamental modes, and one incident angle. Either all or part of the scattering angles are used, which is referred to as a full or partial scattering pattern, respectively. Additional calculations are also made to demonstrate that the accuracy of the results can be improved when more incident angles of the scattering matrix are used.

A. Elliptical flat-bottomed holes

First, flat-bottomed holes are considered and simulations are made with the analytical model. Contrary to complex defects, their geometry can be described exactly with only a few parameters and, although they are not representative of real defects, they are often used

in an industrial context for calibration purposes. They are ideal to study the sensitivity of the Bayesian approach to parameters such as the amount of collected data (sections A.1-A.4) and measurement error (section A.5).

The parameters to be estimated, $\mathbf{X} = \{p_1, p_2, p_3, p_4\}^T$, are defined such that: p_1 is the major axis of the ellipse, p_2 is its aspect ratio, p_3 is the depth and p_4 is the incident angle ϕ. The full search space of the candidate parameters is defined such that: $P_1 = [0, 50mm]$, $P_2 = [0.25, 1]$, $P_3 = [0, h]$ and $P_4 = [-90°, 90°]$. The search space for the major axis P_1 could be extended beyond 50 mm, but it was chosen to restrict the search below a value of twice the incident wavelength. Note that for the aspect ratio, the minimum value in the search space is 25 %, because the analytical model does not allow accurate solutions to be calculated for smaller values [21]. Moreover, because of the symmetry of the scatterers, it is not necessary to extend the search space below -90° and beyond +90°.

Six different flat-bottomed holes were considered. They are referenced in table 1. The model is used to calculate the scattered field of each cavity, and white noise is added to the scattered modes amplitude in order to simulate experimental data. To be consistent with Eq. (5), Gaussian noise with mean 0 and standard deviation σ, $N(0, \sigma)$ is simulated. For example, in the scattering matrix of mode S_0 the noise is normally-distributed with θ such that:

$$\hat{S}_0(\theta) = S_0(\theta) \left[N(0, \sigma^2/2) + \mathrm{i}N(0, \sigma^2/2) \right]. \tag{17}$$

The acquisition of the scattering matrices for modes A_0 and SH_0 is modeled in the same way. The frequency of investigation is 200 kHz, and the simulations are made in a steel plate of thickness $h = 5$ mm. The material properties are: longitudinal velocity $c_L = 5900$ m/s, shear velocity $c_T = 3230$ m/s, and density $\rho = 7800$ kg/m^3. The incident mode is S_0, which has a wavelength of 26 mm at this frequency. The wavelength of the other 2 modes, SH_0 and A_0, is

16 mm and 12 mm, respectively. In order to satisfy Eq. (1), the maximum dimension in the search space being 100 mm, the scattered field was measured with an angular sampling of 5^o. An example of scattering pattern is shown in figure 2 for cavity # 3. The figure also shows the restricted measuring angles used in sections A.2 and A.4 as red arrows. To calculate an accurate first guess for the MCMC algorithm, the simulated annealing is performed over $N_a = 2500$ iterations. This is followed by the MCMC algorithm over an additional $N = 7500$ iterations, thus making the total number of iterations equal to 10000. Computations were made on a laptop with 16 Gb memory and a clock frequency of 2.6 GHz, using MATLAB. With this configuration, the computational time was 2.5 hours for each inversion.

TABLE I
PARAMETERS OF THE CAVITIES AND THEIR CORRESPONDING SYMBOL IN FIGURE 2

	Diameter (mm)	Aspect ratio	Depth (% of h)	$\phi(^o)$	symbol
Cavity# 1	4	0.60	35	60	$\square$
Cavity# 2	18	0.65	40	0	$\Diamond$
Cavity# 3	22	0.75	25	-60	o
Cavity# 4	9	0.40	60	33	$\triangle$
Cavity# 5	6	0.34	50	30	$\triangledown$
Cavity# 6	10	0.50	75	45	$\star$

A.1 Estimation from the full scattering pattern

In order to study the accuracy of the method in ideal conditions, the parameters are first estimated with the assumption that the full scattering pattern is available, with a realistic noise level set equal to $\sigma = 0.01$. Results are shown in figure 3-a. Errors between the estimated and true parameters are less than 2%, apart for cavity # 1 where it is slightly larger on the aspect ratio (6%). The 90^{th} percentile of the solutions (*i.e.* 90 % of the statistically independent solutions) is within 5% of the estimated parameters, apart for the aspect ratio of cavity # 1 where it is within 10%. The slightly inferior accuracy of the aspect ratio for this cavity is due to its very small diameter (4 mm) compared to the wavelength.

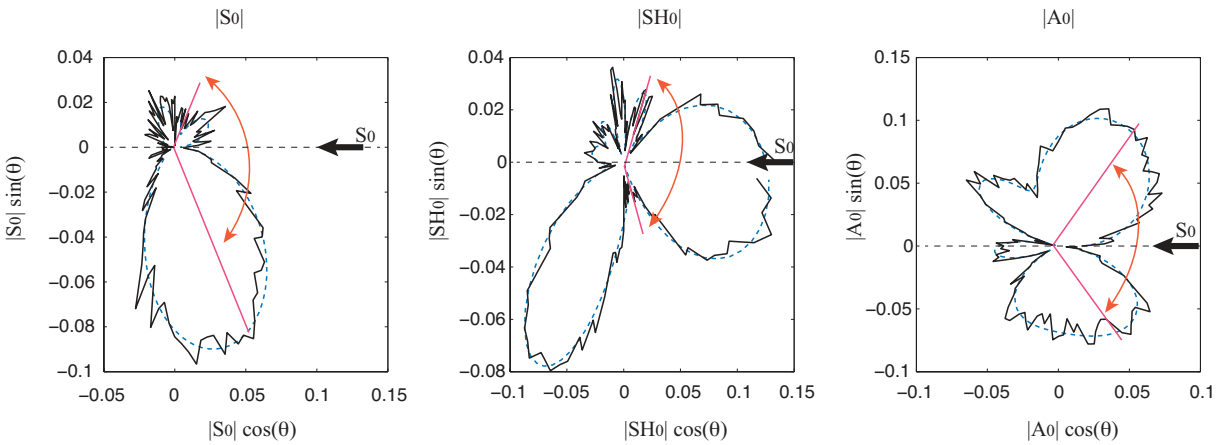

Fig. 2. Far field amplitude of the 3 fundamental modes when the S_0 mode is incident on cavity # 3 in a 5mm steel plate at 200 kHz. Amplitudes are calculated from parameters in table 1 with added white noise as defined in Eq. (17) (solid line) and from the estimated parameters from the posterior distribution of the MCMC (dashed line). The red arrows and straight lines indicate the limits of the measuring angles (*i.e.* -60° and +60°) in the restricted scattering pattern used in sections A.2 and A.4, and the black thick arrows indicate the direction of the incident S_0 mode.

For scatterers with very small dimensions compared to the wavelength, the shape has less influence on the scattered field, because such scatterers start to behave like point sources. Then, small cavities tend to result in similar directivity patterns even if they have different shapes. Overall an excellent agreement can be observed between the true and estimated parameters, and the 90^{th} percentile of the solutions indicates the very good reliability of the results. However, if one is interested in better characterization of the smallest cavities, the difficulty could be overcome by using several incident angles in the scattering matrix, instead of just one. This is demonstrated in the following sections.

A.2 Estimation from partial scattering pattern and 3 modes

Contrary to the previous section, parameters are estimated from part of the scattering pattern of the 3 modes. In order to simulate realistic, on site measuring conditions, it was chosen to limit the amount of data to positions ranging from $\theta = -60°$ to $\theta = +60°$. Results are shown in figure 3-b, and it can be seen that estimation of the parameters remains accurate,

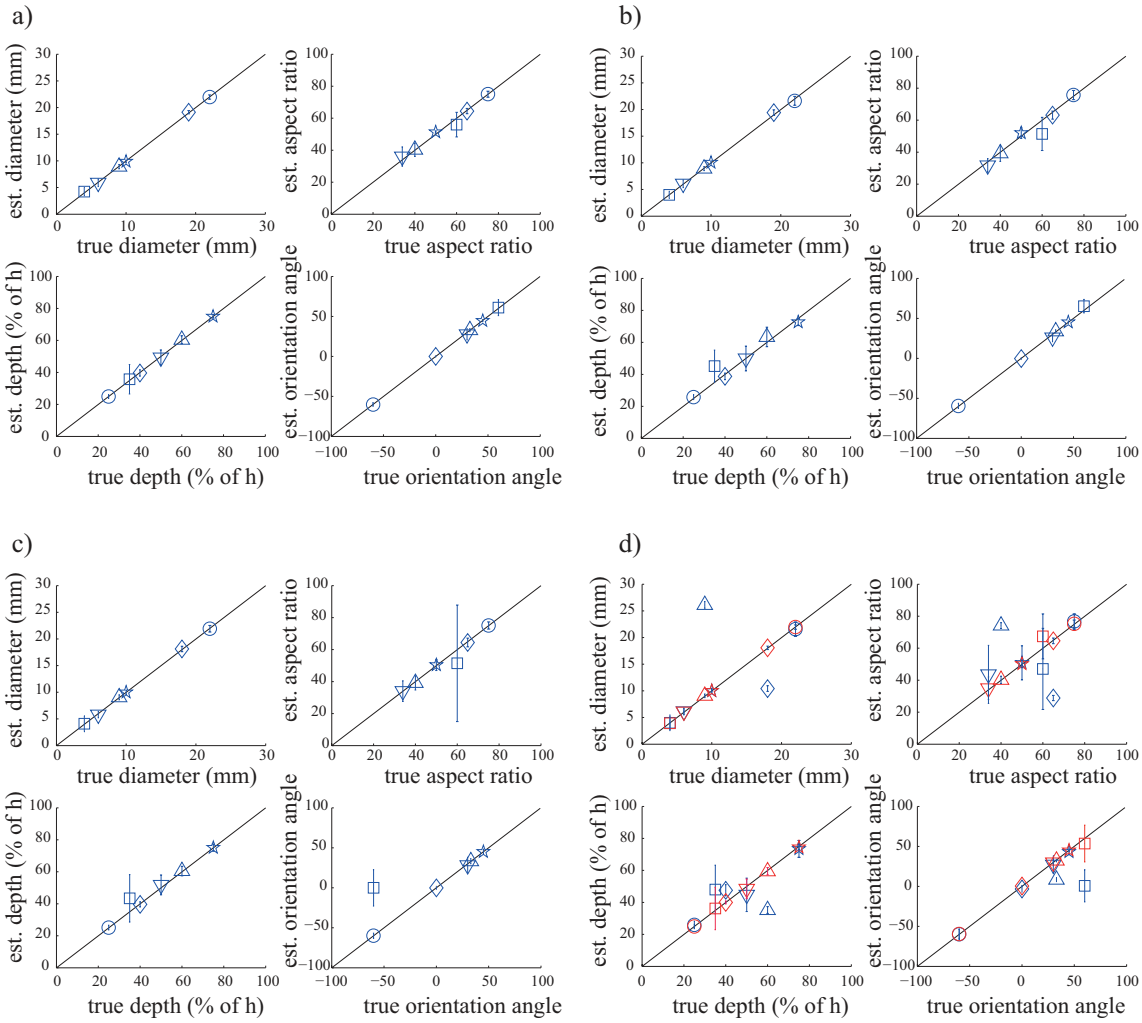

Fig. 3. (color online) Estimated geometrical parameters in the studies of sections A.1-A.4 for the 6 flat-bottomed holes described in table 1: estimations from a) full scattering pattern and 3 modes (section A.1), b) partial scattering pattern and 3 modes (section A.2), c) full scattering pattern and 2 modes (section A.3) and d) partial scattering pattern and 2 modes (section A.4). The red symbols indicate an estimation procedure made with 3 incident angles instead of only one. Error bars represent the 90^{th} percentile (*i.e.* 90% of the statistically independent solutions).

errors with the true parameters being less than 4%, and the 90^{th} percentile being within 8% of the estimated parameters. Accuracy and confidence is however inferior on the depth and aspect ratio of cavity # 1, the error being of 28% and 20%, respectively. This is also due to the small size of this scatterer compared to the incident wavelength, as explained in the previous section.

Note that the lack of data in the partial scattering pattern may be compensated by changing the direction of the incident mode and by measuring a second partial scattering pattern. From an experimental point of view this requires only to change the position of the emitter, and is therefore straightforward to realize. This can be repeated with as many incident angles as desired, thus increasing the amount of data available for the estimation of the defect. If changing the incident angle is not possible, alternative solutions consist of changing another parameter that has influence on the scattering pattern, such as the incident mode or the frequency of inspection. However this is at the cost of increased computational time, because at each iteration of the MCMC algorithm, the number of simulations is equal to the number of incident angles, or to the number of any other parameter that is being changed to collect more data.

For the sake of illustration, compensation using a second incident angle was tested on cavity # 1, which exhibits the most sensitivity to the limitation of measuring positions. Then, instead of calculating the RMS as defined in Eq. (3), in this particular case χ is calculated such that:

$$\chi(\mathbf{X}) = \sqrt{\frac{\left(\chi^{\phi}(\mathbf{X})\right)^2 + \left(\chi^{\phi+\Delta\phi}(\mathbf{X})\right)^2}{2}}, \tag{18}$$

where $\Delta\phi$ is the difference between the two incident angles.

Estimation of the parameters of cavity #1 with two incident angles instead of just 1 allowed a reduction of the errors on the aspect ratio, depth and incident angle to 15 %, 6% and 4%, (down from 20%, 28% and 8%, respectively). The error on the diameter remained unchanged at 0.5%. Moreover, the 90^{th} percentile on the maximum depth and incident angle was also reduced sightly to 13% and 7% (down from 15% and 11%, respectively). The changes on the 90^{th} percentile of the other 2 parameters were negligible. This proves that if computational time is not an issue, accuracy of the estimated defects can be kept to a very

good level despite the generally restricted range of angles available to measure the scattering patterns in a realistic situation.

A.3 Estimation from full scattering pattern and 2 modes

Because not all modes can be measured on-site, this section shows the performance of the method when the scattering pattern of modes S_0 and A_0 alone can be measured. Results are shown in figure 3-c. Performances are similar to those in the previous case (section A.2), in terms of error and confidence interval. Overall very good agreement between the true and estimated parameters can be observed, except again for cavity #1 for which the orientation angle is mis-calculated and the confidence interval on the aspect ratio and depth is not as good.

A.4 Estimation from partial scattering pattern and 2 modes

This configuration corresponds to the worst case. The inversion procedure is performed with modes S_0 and A_0 only, and with a scattering pattern identical to that in section A.2, *i.e.* for measuring positions ranging from $\theta = -60^\circ$ to $\theta = +60^\circ$. The corresponding estimations are shown in blue in figure 3-d. One can see that several parameters are not well estimated, the error with their true value being up to 100% for cavity #4. In that case the problem becomes under-constrained because too much information about the scattered field is missing, which means that some prior knowledge about the scatterer becomes necessary for a good estimation.

It is possible to overcome this difficulty by increasing the number of incident angles, in the way described in section A.2. This solution was then tested with incident angles taking the following 3 values: -60^o, 0^o and 60^o. The corresponding results are shown in red in figure 3-d), and one can see that both accuracy and confidence then become as good as when the

full scattering pattern and 3 modes are used in the inversion process (figure 3-a).

A.5 Sensitivity to noise level

In this section, the robustness of the approach is investigated relative to the noise level. A parametric study is made by varying σ from 0.001 to 0.06. Depending on the size of the geometry, a given noise level may affect differently the solution of the Bayesian procedure. For example a cavity with a small dimension compared to the incident wavelength will not scatter much energy, resulting in signals with a small amplitude and then more likely to a have a poor signal to noise ratio (SNR). Hence for this study to be meaningful, rather than considering noise levels (*i.e.* given values of σ), the SNR will be considered instead. The signal to noise ratio is defined here as a function of the ratio between the power of the scattered modes and that of the noise such that:

$$SNR = 10log_{10}\left|\frac{1/3(E_{S_0} + E_{SH_0} + E_{A_0})}{E_{noise}}\right| \tag{19}$$

where $E_{noise} = 2\pi\sigma^2$, E_{S_0}, E_{SH_0}, and E_{A_0} are the power of the noise and that of the 3 fundamental guided modes, respectively. The power of the modes is calculated as the integral over θ of the square of their amplitude. The SNR associated with the different combinations of cavities and noise levels are referenced in table 2, and one can see that the sensitivity of the method is investigated for values ranging from 0 to 43 dB.

TABLE II
NOISE LEVEL AND THE CORRESPONDING SIGNAL TO NOISE RATIO (IN dB) FOR THE DIFFERENT CAVITIES

	$\sigma = 0.001$	$\sigma = 0.01$	$\sigma = 0.02$	$\sigma = 0.03$	$\sigma = 0.04$	$\sigma = 0.05$	$\sigma = 0.06$
Cavity# 1	25.7	7.3	2.9	1.7	1.1	0.6	0.4
Cavity# 2	37.0	18.1	11.7	9.5	6.6	5.6	4.7
Cavity# 3	33.8	14.2	9.0	6.0	4.7	3.4	3
Cavity# 4	41.8	21.8	16.6	12.7	9.9	8.9	7.3
Cavity# 5	34.6	14.5	9.1	6.1	4.7	3.6	2.8
Cavity# 6	42.9	22.7	16.8	13.1	11.3	9.4	7.7

Results are presented in figure 4, which shows 2 quantities: the error of the results relative to the true values (figure 4-a) and the 95 % confidence interval around the estimated solutions (figure 4-b). For clarity, rather than plotting the error and confidence interval of the 4 parameters individually, instead the mean error and the mean confidence interval are plotted. In both figures the data seem to follow an exponentially decreasing trend, and then a least squares exponential fit of these quantities is plotted (correlation coefficients of 0.78 and 0.89, respectively).

For the interpretation of these results, 3 intervals of SNR are considered:

- zone 1, $0 \leq SNR \leq 5$ dB, representative of very poor measurements quality
- zone 2, $5 < SNR \leq 25$ dB, representative of realistic measurements quality
- zone 3, $SNR > 25$ dB, representative of ideal measurements conditions

Zones 1 and 3 are unrealistic situations because the former represents measurement conditions where the scattering pattern is lost in the noise while the latter represents measurements with negligible noise where the scattering pattern is very clear. See for example the modal directivity for cavity #1 when the SNR is 0.4 dB (figure 4-b) and 26 dB (figure 4-a).

In zone 1, the method allows an estimation of the parameters with an average error less than 45% relative to their true values. However, the confidence interval is not as good, since it spreads within a 80% interval around the estimated solutions. This means that the solution can be approximated with limited accuracy in this regime. This is still a reasonable performance given the very poor SNR in this zone. In zone 2, the method is much more accurate and parameters are estimated with errors comprised between 1% and 10% of their true value, while the 95% confidence interval remains between 4% and 40% of the estimations. As expected, in zone 3 the method performs best, the error of the parameters being less than 1% and the 95% confidence interval being within less than 4% of

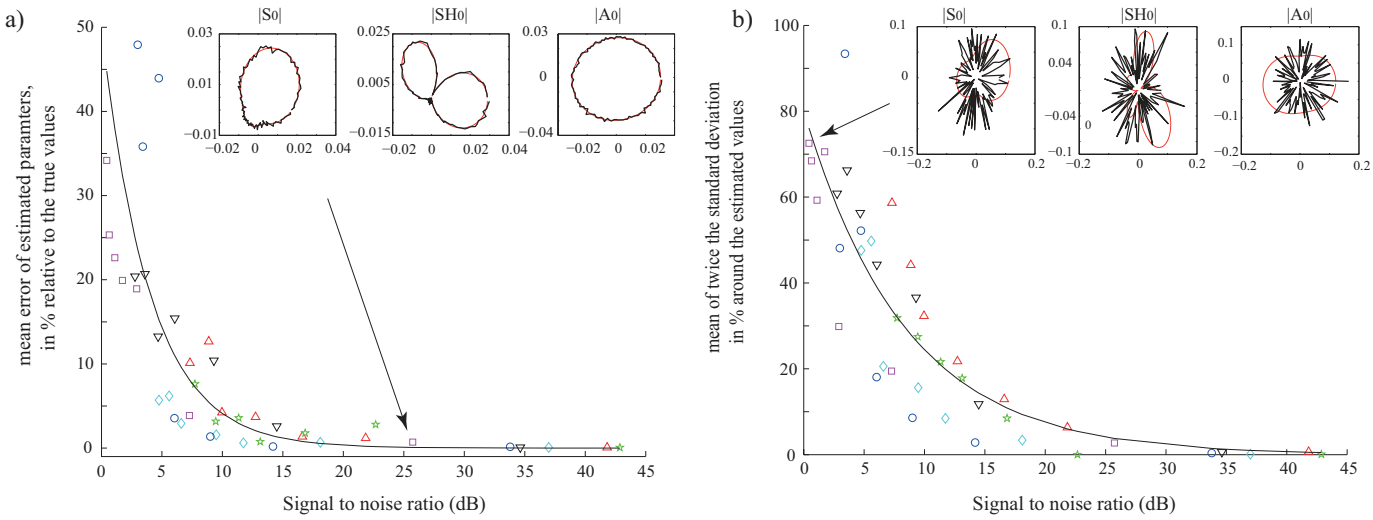

Fig. 4. (Color online) a) Mean relative error and b) 95% mean confidence interval around the solution as a function of SNR. Each symbol represents one of the different defect geometries (table 1) at a given noise level (table 2). The black curve represents an exponential fit of these data. To illustrate the effect of SNR on modal amplitude measurements, the directivity of the scattered modes and their best fit are plotted for cavity #1 when $\sigma = 1e^{-3}$ (left) and $\sigma = 6e^{-2}$ (right)

the estimations. We would like to emphasize that the dimensions of the cavities are all sub-wavelength defects, the smallest having a size of 15% the incident wavelength. Overall the accuracy of the method in the three zones is therefore very encouraging. Given comparable conditions of data acquisition (*i.e.* SNR, quantity of data...), this characterization method seems to outperform current imaging algorithms, such as the linear sampling method, GW tomography and algorithms based on time-of-flight estimation, which are so far unable to provide neither a detailed full 3D description of the scatterers nor a mean of quantifying the uncertainty in the solution.

B. Corrosion defects

In this section, 2 corrosion defects are characterized. Their profile were obtained from laser scans on a steel pipe with a wall thickness of 5mm and outside diameter of 300 mm (courtesy of the Department of Mechanical Engineering at Imperial College London, London, UK). The map of these defects is shown in figures 5-a and 6-a in the form of isolines, the

intensity of which represents the depth of the defect as a percentage of the pipe wall-thickness. Note the presence of a typical, sharp corrosion pit on top of a more extended corroded area. The pit is only initiated in the first defect (at position $X = Y = -5$ mm in figure 5-a, but it can be seen clearly in the second one (at position $X = -10$ mm and $Y = -5$ mm in figure 6-a. This makes the defect very difficult to characterize remotely with guided wave inspection. The maximum depth of the defect, which is the most critical parameter, can generally not be determined and on-site interventions for an eventual repair or replacement of the corroded pipe are decided with empirical criteria. It is therefore essential to be able to provide an accurate estimate of the maximum depth of the defect.

Similarly to the previous section, measurements are simulated by calculating the far field amplitude of the 3 fundamental scattered modes when the S_0 mode is incident, and by adding white noise using Eq. (17). The signal-to-noise ratio is set to 15 dB in both cases. Estimation of the defect profile is made with the full scattering pattern at a frequency of 150 kHz. Then the largest dimension of both defects is less than 75% of the incident wavelength (*i.e.* 35.4 mm at this frequency). Note that for this pipe the wall thickness is small compared to the outside diameter. Moreover, at this frequency its curvature is negligible at the wavelength scale. In these conditions the scattering problem in the pipe is equivalent to that in a steel plate of thickness 5 mm [33]. Therefore simulations are made in a plate rather than in a pipe.

Because a model of flat-bottomed hole cannot fit accurately the geometry of the defects, the FE model is used in this study. Moreover, there is no regular geometry that can describe exactly the complex defects. Therefore, to estimate adequately their geometry with the model, a set of control points is defined. In the plate, the X, Y and Z coordinates of these points define the test parameters in variable $\mathbf{X}^{\mathbf{test}}$. A profile of the candidate defect

is then generated with a 2D spline interpolation of the control points over a 54 x 54 pixels map. The pixel size of the map is 1x1 mm^2 so that it matches that in the laser-scans of the defects. Note that corrosion (*i.e.* the actual defect plus the surface roughness in its immediate vicinity) is modeled only inside this map with the control points that modify the wall-thickness. Outside the map, the Green's function in the FE model is that of a regular stress-free plate, and surface roughness that might be caused by corrosion along the propagation is not taken into account. The simulated annealing is performed over 5000 iterations followed by $N = 15000$ iterations in the MCMC algorithm.

In the model, the mesh is made of tetrahedral elements with a maximum size of 1.5 mm. This size is approximately equal to 1/10 the smallest wavelength in the scattered field (*i.e* that of mode A_0) and 1/25 the largest one (*i.e* that of mode S_0). This choice was made to allow a good compromise between computational costs and accuracy. Computations were made with the same laptop as the one described in the previous section, and each iteration took about 15 seconds, thus making the total calculation time of 80 hours for the 20000 iterations.

For the first defect profile, the number of control points was progressively increased from 1 to 10 by adding 1 control point every 500 iterations in the simulated annealing. For the second defect profile, which has a more complex geometry, the number of control points was increased from 2 to 20 by adding 2 control points every 500 iterations. It is however possible that a more optimal number could be defined. Further investigation is necessary to evaluate the best compromise between accuracy and convergence. The simulated annealing is started at control points with random coordinates X,Y and Z. The next control points are added at random positions X and Y, with their Z coordinate equal to the depth of the last accepted defect profile at these positions. The full search space for the X and Y coordinates of the

control points is $P_{1,2} = [-30mm, 30mm]$ in order to cover dimensions up to twice the incident wavelength, and that of the Z coordinate was $P_3 = [0, 5mm]$. Progressively, all control points converge to the position that best interpolates the true defect.

In the posterior distribution, statistically independent defect profiles are produced by sampling every 50 iterations, as explained in section II-B. The final estimated defect profile is then the average of these profiles at each pixel of the map, so that statistics about the defect can be calculated at critical positions such as that of the maximum depth.

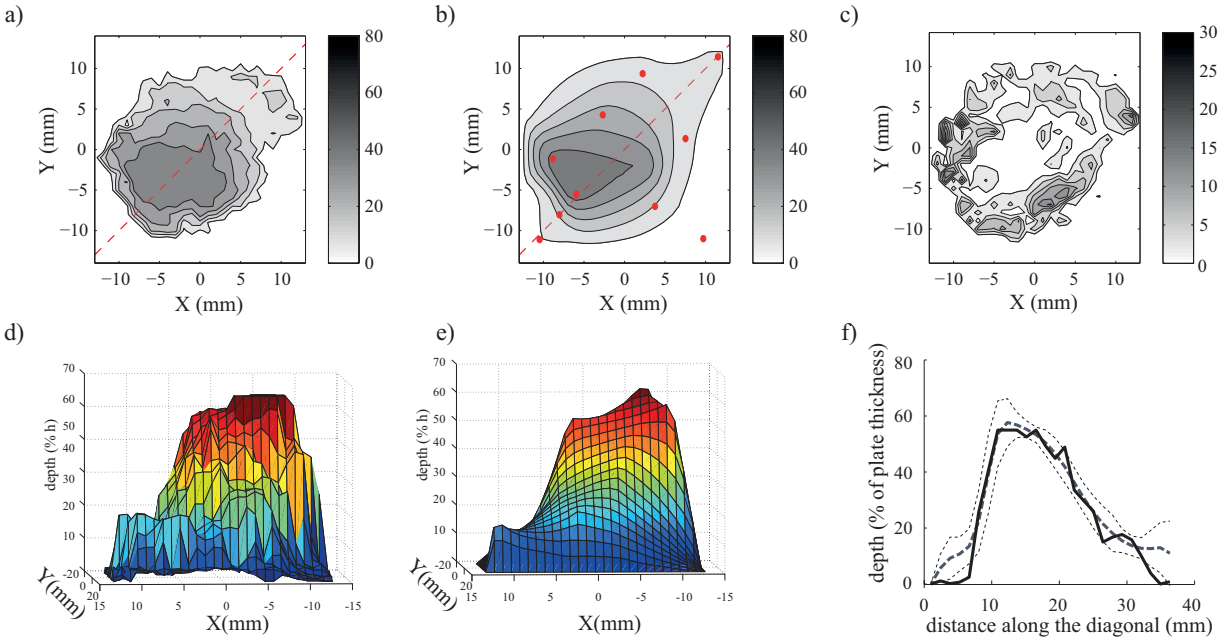

Fig. 5. (Color online) a) and b): map of the true and estimated defect #1, the red dots indicate the mean of the control points in the posterior distribution; c) difference between the 2 profiles. The gray-scale represents the wall-thickness loss in terms of percentage of the total thickness; d) and e) 3D view of the true and estimated defect #1; f) comparison between the true (thick solid line) and estimated (thick dashed line) profiles in the pixels along the diagonal of the map with the standard deviation (thin dashed lines).

Results for the first defect profile are presented in figure 5. Figure 5-a and 5-b show the true and estimated profiles, respectively. The contour of the isolines at the different depths indicate a very good agreement between the 2 profiles, both in terms of dimensions and depth. In particular, the estimated maximum depth is 59% while that of the true defect is

55 %. The error between the 2 profiles is plotted in figure 5-c. It is almost null in the major part of the defect, including at the location of the maximum depth. However it rises up to 20 % of the plate thickness in some pixels located at the edges of the defect. A quantitative comparison between the estimated and true profiles is plotted in figure 5-d, which shows the depth of the defects in the pixels along the diagonal of the map, and the standard deviation. Note the narrow confidence interval, which indicates that the estimated solution is reliable.

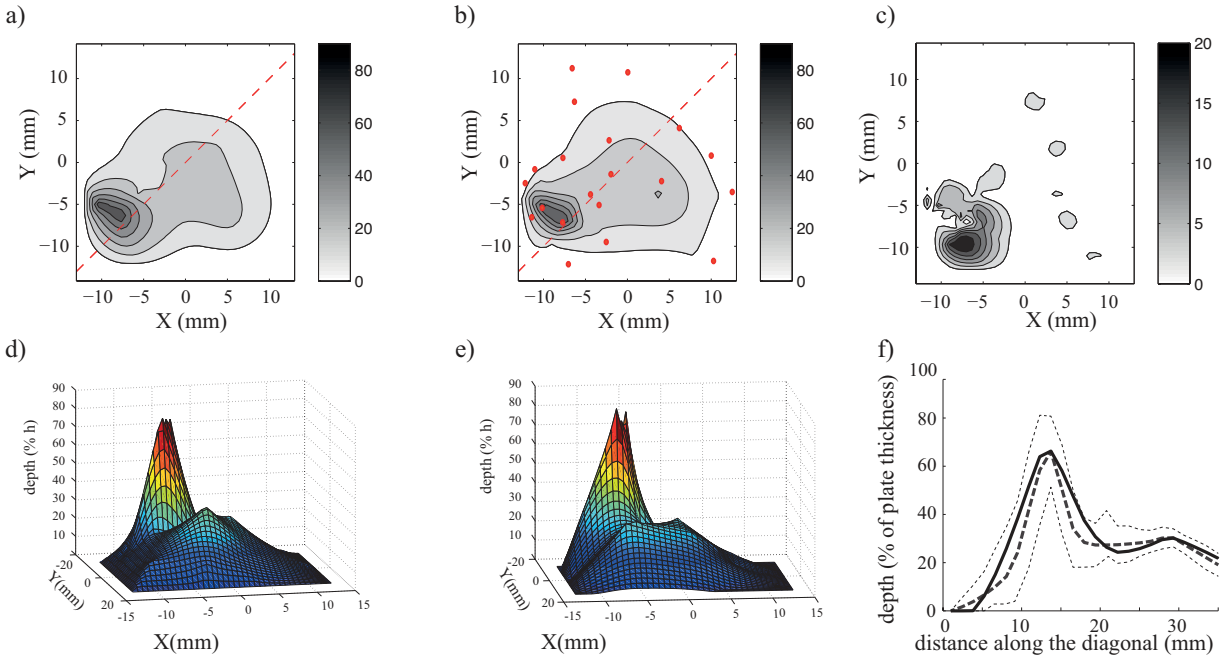

Fig. 6. (Color online) a) and b): map of the true and estimated defect #2, the red dots indicate the mean of the control points in the posterior distribution; c) difference between the 2 profiles. The gray-scale represents the wall-thickness loss in terms of percentage of the total thickness; d) and e) 3D view of the true and estimated defect #2; f) comparison between the true (thick solid line) and estimated (thick dashed line) profiles in the pixels along the diagonal of the map with the standard deviation (thin dashed lines).

Results for the second defect profile are presented in figure 6. The performance of the MCMC algorithm in that case is similar to that in the previous one. Overall the estimated profile (figure 6-b) is in good agreement with the true profile (figure 6-a). The maximum depth is 79% in the estimated profile and 85% in the real one, so it is slightly underestimated. The error between the estimated and true profiles is negligible in the major part of the map

(figure 6-c), except in some pixels at the edges of the defect, where it rises up to 22 %. At the location of the maximum depth, the confidence interval (figure 6-d) is not as good as in the previous case. This could be improved at the cost of increased computational time, by refining the mesh in the FE model so that the sharp pit can be discretized more accurately. The element size of 1.5 mm used in this simulation is indeed not fine enough to accurately account for the sharp geometrical variations in this profile.

The higher error levels at the edges of the profiles is due to the fact that the maps of the real defects have low resolution (*i.e.* 1x1 mm^2). This results in sharp variations of depth from one pixel to the next, which probably do not describe the genuine defects properly. A scan with a finer resolution (*e.g.* 0.25x0.25 mm^2) would provide a smoother and more accurate profile of the actual defects, which would allow a better interpolation of the real geometry. Errors of this type are believed to be of minor importance, because overall the agreement is very good in the major part of the maps, but if one is interested in having a reduced error in all pixels, then the spline-based interpolation may not be the most appropriate method. A radical solution to this problem would consist of running the inversion process by considering each pixel of the map as a parameter, in which case corrosion could be accounted for more finely in the map of the defect. However, with a map of 54x54=2916 pixels, the number of parameters would be too large for a convergence within the 20000 iterations. Moreover, a finer mesh would be required in the model to account for such fine variations in the geometry of the candidate defects, and this is out of the scope of this paper.

V. Experimental Examples

In this section the imaging method is tested on experimental data obtained from an approximately circular flat-bottomed cavity manually machined into a 3 mm thick aluminium plate. In order to avoid unwanted reflections from the edges to interact with the scattered

wave, the dimensions of the plate are 2mx2m (figure 7-a). The depth of the cavity was measured to range from 0.5 to 1 mm and the diameter was 13 ± 1mm (see photo in figure 7-a).

For the acquisition of the data, Electromagnetic Acoustic Transducers (EMAT) connected to a dedicated amplifier were used and controlled with a Matlab interface. The EMATs are specifically designed for the generation and detection of the S_0 Lamb mode and exhibit around 30 dB greater sensitivity to this mode than to A_0 and SH_0 modes. It was not possible to measure the amplitude of the other two modes, because appropriate sensors were not available. The transmitted wave is a 3 cycle Gaussian-windowed sinusoidal wave of central frequency 200 kHz. The transmitting EMAT was located 55 cm away from the centre of the defect so that the wavefront of the incident mode can be considered plane. The receiving EMAT was located in the far field of the defect, 45 cm away from its centre, and moved by hand at positions ranging from -110^o to +110^o of the incident direction axis, with an increment of 5^o. The measured signals were then band-passed filtered and Fourier transformed so that the amplitude of the scattered wave could be evaluated at the central frequency. The resulting θ-dependent amplitude of the scattered S_0 Lamb mode has a SNR of 7 dB, and is plotted in figure 7-b.

In the previous section, no prior knowledge was assumed about the defects, because the scattered fields of at least 2 modes were used to produce an image of the defect. However, only part of the scattered S_0 mode amplitude can be measured in the present case. To compensate for this lack of data, here prior knowledge is assumed about the depth of the hole to perform the inversion. The assumption is that it is less than 2 mm (*i.e.* less than 2/3 of the plate thickness).

First, the analytical model was used, with a cooling schedule and a search space identical

to those in section IV-A. The estimated parameters are: diameter = 14.8 mm ± 2mm; depth = $0.3 \pm 0.1mm$; aspect ratio = 0.92 ± 0.07; orientation = $-7.7^o \pm 6.4^o$. The radius, aspect ratio and orientation are within the measurement errors, but the depth is slightly underestimated. The main reason is the geometry of the machined hole, which is not perfectly flat-bottomed. This results in a lower back-scattered amplitude, which can be identified clearly in figure 7-b in the direction of the incident wave (*i.e.* at 0^o) where the amplitude drops. If the geometry of the hole was perfectly flat-bottomed, then the amplitude of the S_0 mode would be maximum in that direction. Consequently the analytical model is not ideal for this somewhat irregular defect.

A second defect reconstruction was then made from the FE model with the same prior knowledge about the depth. Because the geometry of the defect is a flat-bottomed hole, contrary to the previous section where the distribution of control points was random, here 20 equally spaced control points are defined on a circle, the radius of which is a parameter of the inversion process. The Z coordinate of each control point are parameters as well, so that the model may account for depth variations at the contour of the hole. Moreover, to account for the non-perfectly flat bottom, additional control points are added randomly inside the circle, in a similar way as that of section IV-B. The number of these points is increased progressively from 1 to 10 every 500 iterations over the simulated annealing optimization. The estimated profile is shown in figure 7-c. Its diameter is 12.5 mm and its depth varies between 0.2 mm and 1.2 mm. This is consistent with observations made on the true defect. The best fit of the experimental data is shown in figure 7-b for both the analytical (red dotted line) and FE model (solid blue line). The latter is slightly better, which is confirmed by the value of the RMS between the experimental and modeled scattered field: that of the analytical model is $4.2\text{x}10^{-3}$ V while that of the FE model is $3.6\text{x}10^{-3}$ V. The authors are

confident that the accuracy of the estimated profile could be improved if more data about the scattered field could be collected, for example if the amplitude of the A_0 mode was also measured.

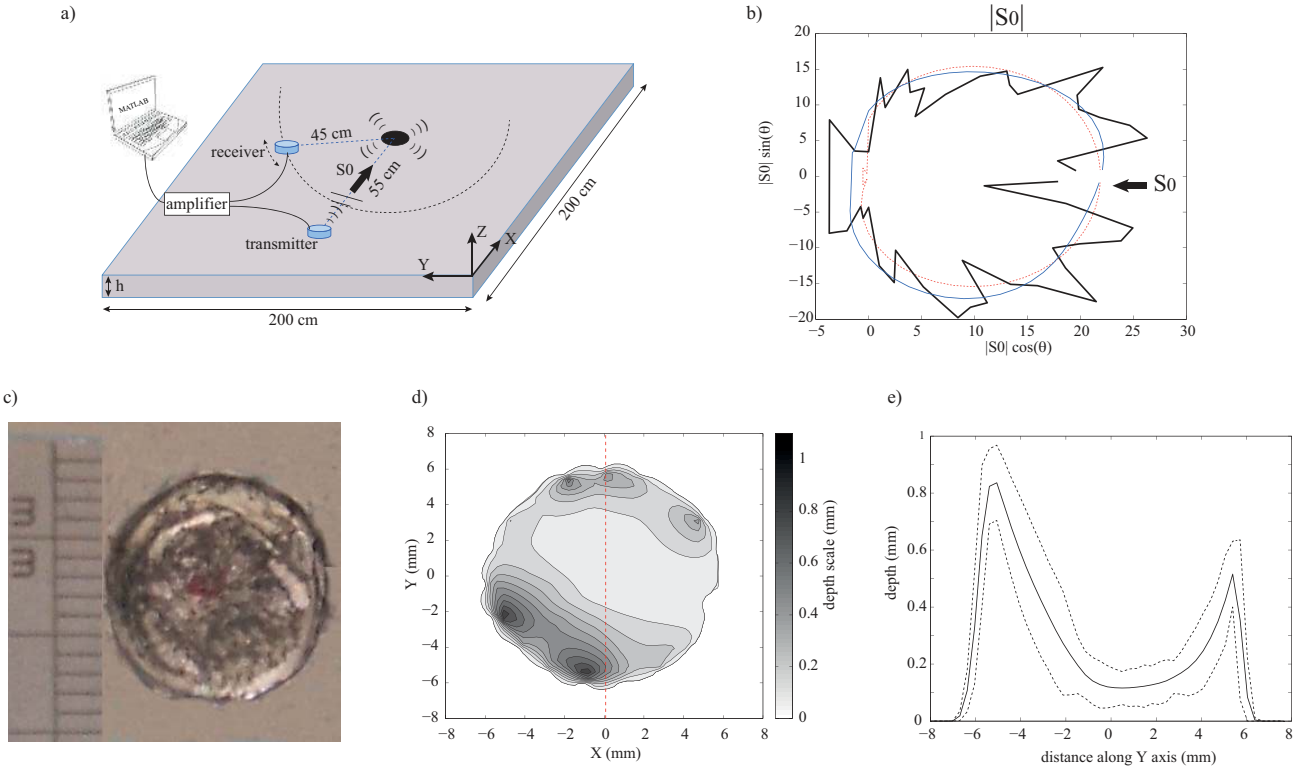

Fig. 7. (Color online) a) Schematic of the experimental setup b) $\theta-$ dependent amplitude obtained from measurements (thick black line) and the best fit from the analytical (red dashed line) and FE (solid blue line) models, c) photography of the drilled hole, d) estimated defect profile from the FE model and e) estimated profile along the pixels of the (O-Y) axis (solid line) with the standard deviation (dotted line).

VI. Conclusions

This paper introduced a Bayesian evaluation method to characterize defects from their scattered fields. The principle of the method is to fit simulated scattered fields to experimental data, which was achieved thanks to a Markov Chain Monte Carlo algorithm used in combination with efficient models. Various sub-wavelength defects such as elliptical flat-bottomed holes or complex corrosion defects were accurately estimated, and for the estima-

tions a good confidence interval was obtained, *i.e.* within about 5% of the solution. The method showed very good robustness to noise, the accuracy and confidence interval both following an exponential decay as a function of SNR. At noise levels typically encountered in NDT (*i.e.* for SNR $\geq$10dB), the error on the geometrical parameters is less than 5%. In addition, a study of the robustness of the method with respect to the amount of data showed that accurate characterization could still be achieved when only partial data about the scattered field is available. In particular, it was shown that when only 1 or 2 of the guided modes can be measured on a restricted range of scattering angles, accuracy and confidence interval can be made as good as when the full scattered field is measured by using just one or two more incident angles in the scattering matrix. However, this paper is an initial demonstration of the approach and the empirical observations about the uniqueness of the reconstructed scatterer based on partial data require further study. For best performance, developing a data acquisition system with the capability to perform measurements of the amplitudes of the 3 modes with good SNR would be an important improvement. The method showed promising results and with optimized coding and computational power, for example using a GPU, it could become a powerful tool to characterize any kind of scatterer. Additional efficiency improvements could be achieved by combining the MCMC algorithm with differential evolution algorithms to optimize the search in the Markov chain for faster convergence. Although the investigations in this paper concerned GW only, this approach can be extended to any scattering problem, including the imaging of multiple scatterers or inspections using bulk waves in medical imaging problems for early characterization of small tumors.

Acknowledgements

This work was supported by EPSRC (Grant no. EP/G052069/1) through the UK Research Centre in NDE, by British Energy, E-on, Shell.

References

[1] P. Cawley, The rapid non-destructive inspection of large composite structures, *Composites 25(5)*, 351–357 (1994)

[2] M. Talmant, J. Foiret, and J. G. Minonzio, Guided waves in cortical bones, in *Bone Quantitative Ultrasound* (Springer, New York, 2010), Chap. 7

[3] P. Kirrmann, On the completeness of Lamb Waves, *J. Elast.* 37(1), 39–69 (1995)

[4] M. V. Predoi, M.Castaings and L. Moreau, Influence of material viscoelasticity on the scattering of guided waves by defects, *J. Acoust. Soc. Am 124(5)*, 2883–94 (2008)

[5] R. Caradente, A. Lovstad and P. Cawley, The influence of sharp edges in corrosion profiles on the reflection of guided waves, *NDTetE Int. 52*, 57–68 (2012)

[6] A. Lovstad and P. Cawley, The reflection of the fundamental torsional mode from pit clusters in pipes, *NDTetE Int. 46*, 83–93 (2012)

[7] B. Mi, J. E. Michaels and T. E. Michaels, An ultrasonic method for dynamic monitoring of fatigue crack initiation and growth, *J. Acoust. Soc. Am 119(1)*, 74–85 (2006)

[8] A. Velichko and P. D. Wilcox, Post-processing of guided wave array data for high resolution pipe inspection, *J. Acoust. Soc. Am 126(6)*, 2973–82 (2009)

[9] L. Bourgeois and E. Luneville, The linear sampling method in a waveguide: a modal formulation, *J. Inverse Problems 24(1)*, 015–018 (2008)

[10] P. Cawley, F. Cegla and M. Stone, Corrosion Monitoring Strategies-Choice Between Area and Point Measurements, *J. Nondestruct. Eval. 32(2)*, 156–163 (2013)

[11] D. Singh, M. Castaings and C. Bacon, Sizing strip-like defects in plates using guided waves, *NDTetE Int. 9*, 394–404 (2011)

[12] N. Metropolis, A. W. Rosenbluth, M. N. Rosenbluth, A. H. Teller and E. Teller, Equation of State Calculations by Fast Computing Machines, *J. Chem. Phys 21*, 1087–91 (1953)

[13] A. Gelman and D. B. Rubin, Markov chain Monte Carlo methods in biostatistics, *Stat. Methods Med. Res. 5(4)*, 339–55 (1996)

[14] D. Creal, A Survey of Sequential Monte Carlo Methods for Economics and Finance, *Econometrics reviews 31(3)*, 245–296 (2012)

[15] Ahmadian, Efficient Markov chain Monte Carlo methods for decoding neural spike trains, *Neural Comput. 23(1)*, 46–96 (2011)

[16] T. Khan and P. Ramuhalli, A recursive bayesian estimation method for solving electromagnetic nondestructive evaluation inverse problems, *IEEE Trans. Magnetics 44(7)*, 1845–55 (2008)

[17] J. Zhang, A. Hunter, B. Drinkwater and P. Wilcox, Monte carlo inversion of ultrasonic array data to map anisotropic weld properties, *IEEE Trans. Ultrason. Ferroelect. Freq. Control 59(11)*, 2487–97 (2012)

[18] O. Fron and A. M. Djafari, A hidden Markov model for Bayesian data fusion of multivariate signals, in *In Fifth Int. Triennal Calcutta Symposium on Probability and Statistics, december 2003*

[19] S. Gautier, G. Le Besnerais, A. M. Djafari and B. Lavayssire, Data Fusion in the Field of Non Destructive Testing, in *Maximum Entropy and B. Methods 79*, 311-316 (1996)

[20] J. Knopp, R. Grandhi, L. Zeng and J. Aldrin, Considerations for Statistical Analysis of Nondestructive Evaluation Data: Hit/Miss Analysis, *E-Journal Adv. Mainten. 4(3)*,

105–115 (2012)

[21] L. Moreau, M. Caleap, A. Velichko and P. D. Wilcox Scattering of guided waves by through-thickness cavities with irregular shapes, *Wave Motion 48(7)*, 586–602 (2011)

[22] L. Moreau, M. Caleap, A. Velichko and P. D. Wilcox Scattering of guided waves by flat-bottomed cavities with irregular shapes, *Wave Motion 49(2)*, 375–387 (2012)

[23] A. Velichko and P. D. Wilcox, A generalized approach for efficient finite element modeling of elastodynamic scattering in two and three dimensions, *J. Acoust. Soc. Am.* 128(3), 1004–14 (2010)

[24] A. Velichko and P. D. Wilcox, Efficient finite element modelling of elastodynamic scattering from near surface and surface breaking defects, in *D. O. Thompson, D. E. Chimenti (editors), Review of Progress in Quantitative and Nondestructive Evaluation* 30, Amer Inst. Physics, Melville, 59–66 (2011)

[25] A. Velichko and P. D. Wilcox, Efficient finite element modeling of elastodynamic scattering with non-reflecting boundary conditions, in *D. O. Thompson, D. E. Chimenti (editors), Review of Progress in Quantitative and Nondestructive Evaluation* 31, Amer Inst. Physics, Melville, 142–149 (2012)

[26] J. Zhang, B. Drinkwater, and P. Wilcox, Defect characterization using an ultrasonic array to measure the scattering coefficient matrix, *IEEE Trans. Ultrason., Ferroelect., Freq.Contr.* 55(10) 2254–2265 (2008).

[27] L. Moreau, A.Velichko, and P. Wilcox, Accurate finite element modelling of guided wave scattering from irregular defects, *NDT&E Int.* 45(1) 46–54 (2012)

[28] C. Andrieu and E. Moulines On the ergodicity properties of some adaptative MCMC algorithms, *The Annals of Applied Probability* 16(3), 1462–1505 (2006)

[29] W. Press, S. Teukolsky, W. Vetterling and B. Flannery, Numerical recipes 3rd edition:

The art of scientific computing, *Cambridge University Press* (2007).

[30] S. Kirkpatrick, C.D. Gelatt Jr and M. P. Vecchi Optimization by Simulated Annealing, *Science* 220(4598), 671–680 (1983)

[31] E. Luneville and J-F. Mercier, Finite element simulations of multiple scattering in acoustic waveguides, *Waves in Random and Complex Media* 20(4), 615–633 (2010)

[32] J. D. Achenbach and Y. Xu Wave motion in an isotropic elastic layer generated by a time-harmonic point load of arbitrary direction, *J. Acoust. Soc. Am. 106(1)*, 83–90 (1999)

[33] A. Velichko and P. D. Wilcox Excitation and scattering of guided waves: Relationships between solutions for plates and pipes, *J. Acoust. Soc. Am.* 125(6), 3623–31 (2009)

Ludovic Moreau was born in Poitiers (France) in 1980. He received a Mres in Aeroacoustics in 2004 from the University of Poitiers (France) and a PhD in Physical Acoustics from the University of Bordeaux (France) in 2007. His thesis was on the interaction between ultrasonic guided waves and scatterers. From 2008 to 2011 he was a research associate in ultrasonic nondestructive inspection at the University of Bristol (England). From 2011 to 2012 he was a research associate in medical acoustics at the University Pierre et Marie Curie in Paris (France). From 2012 to 2013, he was a research scientist in nondestructive testing at CEA in Saclay (France). Since 2013, Dr Moreau has been a lecturer at ISTerre in Grenoble (France), where his current research interests concern the propagation of seismic and ultrasonic waves, ambiant noise correlations, and inverse problems in random and complex media.

Alan J. Hunter was born in Christchurch, new Zealand, in 1978. He received the BE(Hons) and PhD degrees in Electrical and Electronic Engineering from the University of Canterbury, New Zealand in 2001 and 2006 respectively; his thesis was on synthetic aperture sonar data simulation and imaging. From 2006-2007 he was a researcher at the University of Canterbury and from 2007-2010 he was a research associate in ultrasonic non-destructive inspection at the University of Bristol, England. Since 2010, Dr. Hunter has been a research scientist at TNO (The Netherlands Organisation for Applied Scientific Research) in The Hague, where his current research interests are in low-frequency sediment-penetrating sonar, autonomous systems for naval mine counter-measures, passive diver detection sonar, and ultrasonic array imaging for non-destructive inspection.

Alexander Velichko was born in Krasnodar, Russia, in 1975. He received the M.Sc. degree in applied mathematics from the Kuban State University, Krasnodar, Russia, in 1998 and Ph.D. degree from the Rostov State University, Rostov-on-Don, Russia, in 2002. His doctoral research was on investigation of wave fields caused by internal vibration sources in layered elastic medium. From 2005 to 2012, he was employed as a research associate in the Ultrasonics and Non-Destructive Testing Research Group at the University of Bristol. In 2012, he was appointed as a lecturer in the Department of Mechanical Engineering at the University of Bristol, England. His current research interests include mathematical modeling of propagation and scattering of elastic waves, ultrasonic imaging using arrays, and guided waves and signal processing.

Paul D. Wilcox was born in Nottingham (England) in 1971. He received an MEng degree in Engineering Science from the University of Oxford (Oxford, England) in 1994 and a PhD from Imperial College (London, England) in 1998. From 1998 to 2002 he was a Research Associate in the non-destructive testing research group at Imperial College where he worked on the development of guided wave array transducers for large area inspection. From 2000 to 2002 he also acted as a Consultant to Guided Ultrasonics Ltd. (Nottingham, England) a manufacturer of guided wave test equipment. Since 2002 Dr. Wilcox has been at the University of Bristol (Bristol, England) where he is a Professor in Dynamics. His current research interests include long-range guided wave inspection, structural health monitoring, array transducers, elastodynamic scattering and signal processing.